diffusion-fundamentals

The Open-Access Journal for the Basic Principles of Diffusion Theory, Experiment and Application

Solid-State Diffusion and NMR

Paul Heitjans, Sylvio Indris, Martin Wilkening

Universität Hannover, Institut für Physikalische Chemie und Elektrochemie, Germany

Corresponding author:
Paul Heitjans
Institut für Physikalische Chemie und Elektrochemie
Universität Hannover
30167 Hannover, Germany
E-Mail: heitjans@pci.uni-hannover.de

Abstract

Diffusion in solids, which requires the presence of crystal defects or disorder, has both microscopic and macroscopic aspects. Nuclear magnetic resonance techniques provide access to microscopic diffusion parameters like atomic jump rates and activation energies as well as to the tracer diffusion coefficient for macroscopic transport. Microscopic NMR methods include spin-lattice relaxation spectroscopy of stable and beta-radioactive nuclei, spin-spin relaxation or linewidth and spin alignment decay measurements, whereas macroscopic NMR methods are represented by the techniques of static and pulsed field gradient NMR. We recall some basic principles of the mentioned techniques and review case studies for their application to various solids like glassy and crystalline aluminosilicates, nanocrystalline composites, an intercalation compound and a simple bcc metal. Taken together, jump rates in solids are covered over about 10 decades by the microscopic, and diffusion coefficients over 3 decades by the macroscopic NMR methods.

Keywords: Solid-state diffusion, NMR, spin-lattice relaxation, motional line narrowing, spin alignment, SFG NMR, PFG NMR, nanocrystalline composites, aluminosilicates, lithium

1. Introduction

Diffusion in solids, contrary to that in liquids and gases, is only possible if defects, e.g. vacant lattice sites, are present. The site fraction of intrinsic defects in thermal equilibrium increases with temperature and, in a normal crystal, amounts to about 10^{-4} near the melting point as a maximum. As a consequence, diffusion in solids is relatively slow in general. Typically, diffusion coefficients in solids are at most some 10^{-11} m^2/s, whereas in liquids and gases representative values are 10^{-8} m^2/s and 10^{-4} m^2/s, respectively [1]. Exceptionally, in so-called 'solid electrolytes' or 'fast ion conductors', having a high degree of structural disorder, diffusion coefficients may reach values normally found in liquids [2]. Atomic jump rates, representing the microscopic aspect of solid-state diffusion, may range, depending on activation energy and temperature, from

© 2005, P. Heitjans

Table 1. Some microscopic and macroscopic methods for studying diffusion in solids, after [4,5].

	Microscopic	Macroscopic
Nuclear	NMR relaxation, NMR spin-alignment decay, β-radiation detected NMR	Field gradient NMR (static/pulsed)
	Quasielastic neutron scattering	Tracer diffusion
	Mößbauer spectroscopy	
Non-Nuclear	Ionic conductivity (ac)	Ionic conductivity (dc)
	Mechanical relaxation	Mechanical relaxation

about 10^9 s^{-1} near the melting point down to less than 1 s^{-1} in the ultraslow motion regime. It is quite impressive to visualize that in a solid at room temperature, being fairly rigid seen from outside, nevertheless each atom may perform 10^6 jumps per second on average.

Solid-state diffusion can be studied by a large variety of experimental methods [3], which may be subdivided into microscopic and macroscopic ones. Table 1 gives a brief overview [4,5]. Microscopic methods probe diffusion parameters like jump rates of atoms or ions and barrier heights for the jump processes, whereas macroscopic methods are sensitive to long-range diffusion. Microscopic methods are, for example, NMR relaxation spectroscopy, incorporating spin-lattice relaxation as well as spin–spin relaxation or lineshape measurements, spin-alignment decay, β-radiation-detected NMR (β-NMR), quasielastic neutron scattering, Mößbauer spectroscopy, and measurements of the frequency dependent ionic conductivity (including impedance spectroscopy). Examples of macroscopic methods are NMR measurements in a magnetic field gradient (FG-NMR), which may be static or pulsed, tracer diffusion techniques, where concentration profiles in solids are evaluated, dc conductivity measurements and mechanical relaxation spectroscopy in the low-frequency limit. As implemented in Table 1, a further way to classify these diffusion measurement techniques is to distinguish between nuclear and non-nuclear methods. Nuclear methods are those which use radioactive or stable nuclei or elementary particles as probes. Each of the microscopic and macroscopic techniques has its characteristic range in which jump rates and diffusion coefficients, respectively, are accessible (see Fig. 8 in [5]). NMR investigations in solids, to which this article is confined, span the range of jump rates from 10^{-1} to 10^9 s^{-1} in the case of the microscopic methods. Macroscopic NMR techniques cover diffusion coefficients in the range $10^{-14}…10^{-11}$ m^2s^{-1}.

In the following we first briefly recall some basics of solid-state diffusion (Sect. 2) with emphasis on microscopic aspects. Then in Sect. 3 an outline of the various NMR techniques for probing elementary diffusion jumps, including the β-NMR method, is given. Furthermore, some notes on principles of field gradient NMR measuring

macroscopic transport in solids are presented. Finally in Sect. 4 we review case studies from our own laboratory where the above NMR methods have been employed.

2. Basics of Solid-State Diffusion

Diffusion is the process of particle movement driven by a concentration gradient [6]. Fick's first law relates the particle flux $\boldsymbol{j}_\mathrm{p}$ to the gradient of concentration c of these particles:

$$\boldsymbol{j}_\mathrm{p} = -D^\mathrm{T}\nabla c \quad . \tag{1}$$

D^T is the tracer diffusion coefficient or diffusivity. Combining Eq. (1) with the continuity equation

$$\frac{\partial c}{\partial t} + \nabla \boldsymbol{j}_\mathrm{p} = 0 \tag{2}$$

results in Fick's second law:

$$\frac{\partial c}{\partial t} = \nabla\left(D^\mathrm{T}\nabla c\right) \quad . \tag{3}$$

This partial differential equation simplifies if D^T is constant and can be solved for particular initial and boundary conditions [7]. This allows one to determine D^T from measurements of concentration profiles $c(\boldsymbol{r},t)$. The temperature dependence of the diffusion coefficient is often described empirically by an Arrhenius relation

$$D^\mathrm{T} = D_0^\mathrm{T} \cdot \exp\left(-\frac{E_\mathrm{A}}{k_\mathrm{B}T}\right) \tag{4}$$

where E_A is the activation energy for the mass transport, $D_0{}^\mathrm{T}$ is the pre-exponential factor, k_B is is the Boltzmann constant and T is the temperature.

From the microscopic point of view, the tracer diffusion coefficient D^T can be defined by the Einstein–Smoluchowski relation [8,9]

$$D^\mathrm{T} = \lim_{t\to\infty} \frac{\left\langle r^2(t)\right\rangle}{2dt} \quad . \tag{5}$$

Here $\langle \boldsymbol{r}^2(t)\rangle$ is the mean square displacement of the particles after the time t and d is the dimensionality of the movement. An atom moving through a solid will perform jumps between different minima in a potential landscape. In crystalline solids these minima are represented by lattice sites or interstitial sites. In general, the potential landscape may be time dependent [10,11]. Considering the case where the mean jump time is short compared to the mean residence time τ in such a minimum, the trajectory of a particle is composed of a sequence of elementary jumps with average jump length ℓ. From these microscopic quantities a diffusion coefficient D^uc for uncorrelated jumps can be defined by

$$D^\mathrm{uc} = \frac{\ell^2}{2d\tau} \quad . \tag{6}$$

The diffusion coefficients D^T and D^uc are related by

$$D^\mathrm{T} = f \cdot D^\mathrm{uc} \tag{7}$$

where f is the correlation factor. f equals unity if the movement is purely random hopping. For correlated motion of the atoms with enhanced backward hopping probability after completed jumps one has $0 < f < 1$. In favourable cases the experimentally determined correlation factor can yield information about the diffusion mechanism. In structurally ordered, i.e. single crystalline systems defects are required for the movement of atoms or ions. The concentration of point defects in thermal equilibrium is governed by statistical thermodynamics [12]. Starting from a single crystal, the introduction of defects and thus disorder leads to increasingly defective systems, i.e. so-called highly defective single crystals, micro/nanocrystalline materials and amorphous systems, which cover the range from disorder on regular sites to structural or topological disorder. The defects can be zero-dimensional (e.g. vacancies or interstitials), one-dimensional (dislocations) or two-dimensional (grain boundaries) defects. The highest degree of disorder can be found in amorphous materials. One point of interest is to investigate whether there is a correlation between structural disorder and the appearance of fast diffusion.

3. NMR Methods

3.1 Microscopic Methods

Spin-Lattice Relaxation

Diffusion can be probed by spin-lattice relaxation (SLR) caused by the temporal fluctuations of local fields due to the motion of particles carrying a nuclear spin. The principle can be understood from the simple picture of a probe spin precessing in an external magnetic field $\boldsymbol{B}_0$ with a Larmor precession frequency ω_L given by $\omega_L = \gamma B_0$, where the magnetogyric ratio γ connects nuclear magnetic moment and angular momentum. The nuclear spin will be reversed, i.e. the transition probability will be maximum, when ω_L is in resonance with the frequency of a transverse alternating field B_1. This may be an external radio-frequency field or the internal fluctuating field due to the motion of the atoms. In the following the latter case will be regarded more closely.

The fluctuating field which may be dipolar magnetic from neighbouring nuclei as well as quadrupolar electric from local electric field gradients can be described by the correlation function $G(t)$ which contains the temporal information on the atomic diffusion process [13-15]. The correlation time τ_c characterizing $G(t)$ is within a factor of the order of unity equal to the mean residence time τ between successive atomic jumps. Relevant for SLR is the spectral density function $J(\omega)$ of the fluctuating local field which is the Fourier transform of the correlation function $G(t)$ and extends up to frequencies of the order of τ_c^{-1}. Transitions between the energy levels of the spin system will be induced, i.e. spin-lattice relaxation becomes effective, when $J(\omega)$ has components at the transition frequencies. The spin-lattice relaxation rate T_1^{-1}, being a measure of the transition probability, is given for a nucleus with spin quantum number I by

$$T_1^{-1} = \frac{3}{2}\gamma^4\hbar^2 I(I+1)\left\{J^{(1)}(\omega_L) + J^{(2)}(2\omega_L)\right\} \tag{8}$$

where $\hbar$ is the Planck constant divided by 2π. $J^{(q)}(\omega)$ (q = 0,1,2) denote spectral densities which result in transitions of spin pairs, where the combined angular momentum changes by $q\hbar$. The basic characteristics of T_1^{-1} in a 3D system with random jump diffusion can be derived from the simple exponential correlation function

$$G^{(q)}(t) = G^{(q)}(0) \cdot \exp\left(-|t|/\tau_c\right) \tag{9}$$

assumed by Bloembergen, Purcell and Pound (BPP) [16]. The corresponding Lorentzian shaped spectral density function is given by

$$J^{(q)}(\omega) = G^{(q)}(0) \cdot \frac{2\tau_c}{1+(\omega\tau_c)^2} \quad . \tag{10}$$

The correlation time τ_c, like the mean residence time τ, will generally show Arrhenius behaviour (cf. Eqs. (4) and (6)). $T_1^{-1}(T)$, measured at a certain Larmor frequency ω_L, passes through a maximum at a specific temperature which is determined by the condition $\omega_L \cdot \tau_c \approx 1$. In the usual representation of log T_1^{-1} vs. $1/T$ the peak for each Larmor frequency is symmetric. At temperatures above and below the maximum the slopes yield the activation energy E_A. The SLR rate shows no ω_L dependence in the high-T limit and follows the power law $T_1^{-1} \propto \omega_L^{-2}$ in the low-T limit.

In real solids, the standard behaviour of T_1^{-1} for uncorrelated 3D diffusion, sketched above, is rarely observed in detail. Mostly, log T_1^{-1} vs. $1/T$ is asymmetric with a smaller slope on the low-T side, which indicates correlated diffusion. This has been ascribed to the influence of disorder and Coulomb interaction between the ions [10]. If diffusion is low-dimensional, the slope of log T_1^{-1} vs. $1/T$ in the high-T limit should be smaller than in the BPP case and specific dependences of T_1^{-1} on ω_L are expected for 2D and 1D diffusion.

If spin-lattice relaxation is not probed with reference to the static external field $\boldsymbol{B_0}$ but in a resonant alternating field $\boldsymbol{B_1}$, the SLR rate in the rotating frame, $T_{1\rho}^{-1}$, is measured. Since $B_1 \ll B_0$, the condition for the maximum of the SLR rate entails that considerably longer correlation times are probed than by T_1^{-1} measurements. For details we refer to [17].

β-Radiation Detected NMR

Besides stable nuclei, normally employed in NMR, beta-radioactive nuclei can also be used as probes for NMR (β-NMR) [18], in particular for unconventional SLR measurements. The principle of β-NMR relaxation is the use of the β-decay radiation asymmetry of polarized, short-lived β-emitters embedded in the solid in order to monitor the nuclear polarization and its decrease due to longitudinal, i.e. spin-lattice relaxation [4]. It includes (i) on-line production of the short-lived polarized probe nuclei with lifetimes τ_β ranging from some 10 ms to some 100 s, and (ii) in-situ measurement of the β-asymmetry during a subsequent time interval of a few lifetimes. The signal amplitude resulting from step (i) is determined by the angular distribution of the emission probability $W(\theta)$ of β-particles from an ensemble of polarized β-active nuclei into a solid angle element at angle θ between polarization and emission direction:

$$W(\theta) = 1 + P\cos\theta \quad . \tag{11}$$

P is the nuclear polarization characterized by a linearly varying population of the Zeeman levels. The β-decay radiation asymmetry a_β, which is given by the 0°-180°-difference of $W(\theta)$, is a direct measure of P and reflects any changes of it.

The polarized β-emitters can be produced on-line by various nuclear reaction schemes [17]. Here we mention only the β-NMR technique using the capture of polarized reactor neutrons [19]. The sample abundantly containing the nuclei for the production reaction is placed in the field $\boldsymbol{B}_0$ of an electromagnet and irradiated with polarized cold neutrons. For example, in the case of the probe nucleus ^{8}Li, the reaction is

$$\vec{n} + {}^7\mathrm{Li} \rightarrow {}^8\vec{\mathrm{Li}}^{\,*} \xrightarrow{\gamma} {}^8\vec{\mathrm{Li}} \xrightarrow{\beta^-} 2\alpha \quad . \tag{12}$$

Established probe nuclei available with the neutron capture technique are: ^{8}Li (τ_β=1.2 s), ^{12}B (29 ms), ^{20}F (16 s), ^{23}Ne (57 s), ^{28}Al (3.2 min), ^{108}Ag (3.5 min), ^{110}Ag (35 s), ^{116}In (20 s).

The β-particles are detected by β-scintillators mounted on the pole faces 'North' and 'South' of the electromagnet. The corresponding counting rates Z_N and Z_S at $\theta = 0°$ and 180°, respectively, yield the experimental β-asymmetry

$$a_\beta = \frac{Z_N - Z_S}{Z_N + Z_S} \quad . \tag{13}$$

As pointed out above, a_β is proportional to the nuclear polarization P. β-NMR relaxation measurements are performed by monitoring transients $a_\beta(t)$ after neutron activation pulses generated with a chopper. In simple cases monoexponential transients

$$a_\beta(t) = a_{\beta 0} \cdot \exp(-t/T_1) \tag{14}$$

with the SLR time T_1 are observed.

Special features of the β-NMR method with respect to SLR measurements are as follows. The polarization P is high and independent of a Boltzmann factor. Thus low values of the magnetic field (which provides the quantization axis) and high temperatures are accessible. The concentration of the probe nuclei is extremely small (typically 1 in 10^{18} other nuclei) and as a consequence spin diffusion, i.e. the polarization transfer by resonant mutual spin flips of like nuclei, is suppressed due to their large distance. Thus SLR by distant paramagnetic impurities, generally effective via spin diffusion in classical NMR relaxation measurements, does not contribute to β-NMR relaxation. The highly diluted probe nuclei relax individually and the β-asymmetry signal stems from an inhomogeneous polarization average of the probe nuclei. A technical advantage of β-radiation detected SLR is that no radiofrequency irradiation is required. The field B_0, correspondingly the Larmor frequency of the measurement, is easily variable and skin effect problems do not arise. Bulk metallic samples and/or metallic sample containers can be used. The latter is often desirable when corrosive materials are to be studied. The measurement of SLR times T_1 is restricted to a time window of at most $0.01\,\tau_\beta < T_1 < 100\,\tau_\beta$.

Line Narrowing

In addition to SLR measurements also measurements of the overall NMR linewidth of the central transition (+1/2 ↔ -1/2) as a function of temperature can be used to explore

microscopic diffusion parameters [17]. The NMR linewidth is related to the spin-spin relaxation rate T_2^{-1} which, in terms of the spectral densities $J^{(q)}$, reads

$$T_2^{-1} = \frac{3}{8}\gamma^4\hbar^2 I(I+1)\left\{J^{(0)}(0) + 10J^{(1)}(\omega_L) + J^{(2)}(2\omega_L)\right\} \quad . \tag{15}$$

Eq. (15) accounts for homonuclear dipole-dipole interactions between the nuclear spins only. Assuming, as in the case of T_1^{-1}, an exponential correlation function $G^{(q)}$ [16] (cf. Eq. (9)), the spectral densities are Lorentzian shaped functions again (Eq. (10)). If the correlation rate τ_c^{-1} is much smaller than the Larmor precession frequency ω_L, T_2^{-1} is approximately given by

$$T_2^{-1} \propto J^{(0)}(0) \propto \tau_c \quad . \tag{16}$$

Eq. (16) holds only for $J^{(0)}\tau << 1$, or $G^{(0)}\tau^2 << 1$ (see below). This condition is violated at low temperatures, when jump rates are much less than the transverse relaxation rate, i.e. in the limit $G^{(0)}\tau^2 >> 1$. In that case, the nuclear spins in an external magnetic field $B_0 = \gamma/\omega_L$ experience slightly different dipolar interactions leading to a distribution of resonance frequencies around the mean value ω_L. In the case of, e.g., an amorphous homogeneous solid, the frequency distribution is Gaussian like and shows up in a broadened central transition. In this temperature range one obtains for T_2^{-1} the so-called *rigid-lattice* result

$$T_{20}^{-1} \propto \left(G^{(0)}\right)^{1/2} = \text{const.} \tag{17}$$

When the sample is heated the ions start moving through the solid and local magnetic fields are averaged out. Thus, the transverse relaxation process is slowed down and as a consequence the NMR line starts to narrow when jump rates are of the order of the rigid-lattice linewidth. In this *motional narrowing* regime T_2^{-1} is given by Eq. (16). Accessible jump rates are in the range between 10^3 s^{-1} and 10^5 s^{-1}, depending on the strength of dipolar interactions between the spins.

At much higher temperatures, when τ^{-1} exceeds the Larmor frequency, $J^{(1)}(\omega_L)$ and $J^{(2)}(2\omega_L)$ start to contribute significantly to transverse relaxation and the temperature dependence of T_2^{-1} follows that of T_1^{-1}. In this *extreme motional narrowing* regime, the temperature independent residual linewidth is due to inhomogeneities of the external magnetic field B_0.

Spin-Alignment NMR

Ionic motions on the ultraslow time-scale with jump rates in the kHz to sub-Hz range, are hardly accessible by recording lineshapes or spin-spin relaxation times, because ultraslow motions do not or only marginally affect the lineshape, as explained above. However, the measurement of multiple-time correlation functions can be used to investigate ultraslow translational ionic jumps in solid ion conductors [20]. Spin-alignment echo (SAE) NMR spectroscopy, developed for deuterons [21] with spin quantum number $I = 1$, was quite recently applied to study ion dynamics using spin-3/2 quadrupole nuclei like ^{9}Be [22,23] and ^{7}Li [23-26].

Spin-alignment echo NMR spectroscopy probes diffusion by labelling the ions via their quadrupole frequency

$$\omega_Q / 2\pi = e^2 qQ / 4h \cdot \left(3\cos^2\Theta - 1 - \eta \sin^2\Theta \cos(2\Phi)\right) \tag{18}$$

which is due to the interaction between the nuclear quadrupole moment and a non-vanishing electric field gradient (EFG) at the nuclei site. Here e is the proton charge, Q the electric quadrupole moment of the nucleus, q the EFG and η the EFG asymmetry parameter. The polar angles Θ and Φ denote the orientation of the external magnetic field in the principal axis system of the EFG tensor. The quadrupole interaction alters the Zeeman frequency $\omega_L/2\pi$ according to $\omega_L \pm \omega_Q$. Provided electrically inequivalent sites are visited within a given diffusion pathway by the jumping ion, the information about the dynamic process is coded in terms of a change in the quadrupole frequency ω_Q.

The spin-alignment technique allows one to measure directly a single-particle correlation function yielding information about dynamic as well as geometric parameters of the hopping process. The pulse sequence used to sample spin-alignment echos is based on the three-pulse sequence of Jeener and Broekaert [27],

$$\beta_{1,\phi 1} - t_p - \beta_{2,\phi 2} - t_m - \beta_{1,\phi 3} - t \quad ,$$

with $\beta_1 = 90°$ and $\beta_2 = \beta_3 = 45°$. ϕ_i denotes the phase of the respective pulse. Starting from the magnetization in thermal equilibrium, the first two pulses generate, if $|\phi_1 - \phi_2| = 90°$, the quadrupolar alignment state [28]. The reading pulse after a mixing period t_m transforms spin-alignment back into an observable transverse magnetization leading to an echo at $t = t_p$. With the pulse lengths mentioned above the echo amplitude S_2 is maximal and is given by [28]

$$S_2(t_p, t_m, t) = \frac{9}{20}\left\langle \sin\left[\omega_Q(0)t_p\right] \sin\left[\omega_Q(t_m)t\right]\right\rangle \quad . \tag{19}$$

Angular brackets $\langle \ldots \rangle$ denote powder average. Appropriate phase cycling [24,28] is necessary in order to pick out the correct coherence pathway and to eliminate unwanted coherences as well as to reduce the effects of pulse imperfections.

The decay of the alignment echo amplitude $S_2(t_p,t_m)$ at $t = t_p$ and for fixed evolution time t_p and as a function of mixing time t_m is in general due to two processes, i.e. (i) individual jumps of the ions and (ii) longitudinal relaxation. The first one, characterized by the decay constant τ_{SAE} being directly related to the motional correlation time, will affect the echo formation when the ions are jumping between inequivalent sites. Simultaneously, the second process gives rise to a decay of the longitudinal order and thus to a decrease of the alignment echo amplitude, too. Therefore the experimental time window to investigate ionic motions is limited by longitudinal relaxation, i.e. $\tau_{SAE} < T_1$.

3.2 Macroscopic Methods

SFG NMR

In an SFG NMR experiment a spin echo experiment is performed in a time independent magnetic field gradient of magnitude g. In the case of solids, strong gradients of some tens T/m are needed. These can be found in the stray field of conventional cryomagnets, as pointed out by Kimmich et al. [29]. The gradient direction is defined to be the z-direction ($B = B_0 + g\ z$). After a $\pi/2$ pulse has turned the

magnetization into the *x*-*y*-plane, the magnetization starts precessing around the B_0 field direction (*z*-direction). Because of the presence of the spatially dependent magnetic field the magnetization has a spatially dependent precession frequency. This results in a continuously increasing phase difference $\phi(t)$ depending on the spatial position of the nuclei along the axis parallel to the gradient direction. At time τ_e, a π pulse inverts the direction of the magnetization in the *x*-*y*-plane, whereas the direction of the gradient field does not change and therefore the phase difference starts to decrease according to

$$\phi(2\tau_e) = \gamma \int_0^{\tau_e} z\, g(t')\, \mathrm{d}t' - \gamma \int_{\tau_e}^{2\tau_e} z\, g(t')\, \mathrm{d}t' \quad . \tag{20}$$

The phase difference, having evolved during the time interval between the π/2 and the π pulse, can be compensated in the time interval between the π pulse and the echo appearance at time $2\tau_e$ if there is no diffusion. In this case the spin echo amplitude is only damped due to T_2 relaxation as it would occur in a usual spin echo experiment. If translational diffusion, i.e. atomic transport, takes place, the echo is additionally damped [30,31]. The damping is then governed by the magnitude of the field gradient *g* and the duration $2\tau_e$ of the experiment. Since the gradient is not changed the only variable parameter is the experiment duration $2\tau_e$. Changing $2\tau_e$ gives a contribution to echo damping from T_2 relaxation which has to be corrected for. Possibilities are (i) the determination of T_2 in a separate measurement, (ii) fitting the magnetization decays due to diffusion and T_2 relaxation simultaneously or (iii) using more complex pulse sequences [32].

In solids T_2 can be very short. Since the experiment duration is limited by T_2, it is very often too short to get a noticeable echo damping caused by diffusion. Then the stimulated spin echo (STE) pulse sequence is more appropriate than the simple Hahn spin echo sequence often used for liquids [33]. In an STE pulse sequence the π pulse is split into two π/2 pulses. Between these π/2 pulses the magnetization is stored parallel to the *z*-axis. Because T_2 relaxation only affects the component of the magnetization in the *x*-*y*-plane there is no T_2 relaxation in the time between the split π pulse, there is only T_1 relaxation. In solids T_1 is usually much longer than T_2. Therefore, the available time window of an STE experiment for observing diffusion is enlarged. For the STE experiment echo damping is given by [33]

$$\frac{M(\tau_1+\tau_2)}{M(0)/2} = \exp\left(-\frac{\tau_2-\tau_1}{T_1} - \frac{2\tau_1}{T_2} - D^{\mathrm{T}}\gamma^2 g^2 \tau_1^2 \left(\tau_2 - \frac{\tau_1}{3} \right) \right) \quad . \tag{21}$$

$M(\tau_1+\tau_2)$ and $M(0)$ are the values of the macroscopic magnetization at the echo appearance time $\tau_1+\tau_2$ and at t=0. τ_1 and τ_2 are the delay times of the second and third π/2 pulse, respectively, with respect to the first π/2 pulse.

PFG NMR

In PFG NMR gradient pulses $g(t)$ are inserted between the radio frequency pulses of a Hahn spin echo sequence. After application of a π/2 pulse the magnetization precesses perpendicular to the B_0 field. Then the first gradient pulse labels the nuclei within the sample with respect to their spatial position along the *z*-axis parallel to the gradient

direction. This means that the first gradient pulse causes a phase difference $\phi(z,g)$ of the precessing magnetization. After a delay time τ_e a π pulse inverts the direction of the magnetization in the *x*-*y*-plane. Then a second gradient pulse is applied which compensates for the phase difference gained during the first gradient pulse. Disregarding the T_2 relaxation, the compensation can be complete only if there is no diffusion during the time Δ between the two gradient pulses. Δ is denoted as observation time. If there is diffusive transport of the nuclei during Δ, the echo amplitude is damped [34-36]. The damping is governed by the tracer diffusion coefficient D^T, the observation time Δ, the magnitude g of the gradient pulses and their duration δ. As mentioned before, in case of small T_2, i.e. in solids, it is more suitable to apply an STE pulse sequence. In an STE pulse sequence the gradient is applied between the first and the second π/2 pulse as well as after the third π/2 pulse. The echo damping is then given by

$$\frac{M(\tau_1+\tau_2)}{M(0)/2} = \exp\left(-\frac{\tau_2-\tau_1}{T_1}-\frac{2\tau_1}{T_2}-D^T\gamma^2 g^2\delta^2\left(\Delta-\frac{\delta}{3}\right)\right) \quad . \tag{22}$$

This equation holds if (i) the observation time Δ is long compared to the duration δ of the gradient pulses (short gradient pulse approximation, $\Delta >> \delta$) and (ii) the diffusion process is random (Gaussian probability density) [37].

4. Case Studies

4.1 Spin-Lattice Relaxation: ^{7}Li and ^{8}Li in Glassy and Crystalline Spodumene

As an example for a comparative study of long-range and local ionic motion in a glass as well in the corresponding crystalline material both by NMR and β-NMR relaxation, we present results on Li motions in the spodumene ($LiAlSi_2O_6$) system. In the crystal structure of β-spodumene there are four pairs of closely neighboured Li sites per unit cell. Their distance is 0.13 nm and only one site is occupied at a time. The distance between different pairs of Li sites is about 0.45 nm. This suggests two types of possible Li jumps,

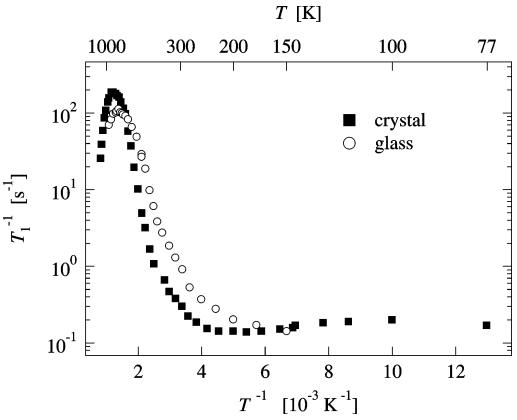

Fig.1: Temperature dependence of T_1^{-1} of ^{7}Li in glassy and polycrystalline $LiAlSi_2O_6$ (β-spodumene) at $\omega_1/2\pi$ = 38.9 MHz [17,38].

long-range jumps between different pairs and a localized motion by hops between the sites of a pair.

In Fig.1, ^{7}Li $T_1^{-1}(T)$ data for the glassy and the crystalline sample at one frequency are compared [17,38]. For both modifications a pronounced diffusion-induced peak shows up which in the case of the glass occurs at roughly 700 K, i.e. some 250 K below the glass transition temperature, and in the case of the crystal at about 820 K. These peaks are due to the long-range Li jumps. The temperature values of the T_1^{-1} maxima and the slopes of the low-T flanks show that the jump rate of Li^+ is faster and the activation energy is smaller in the glass than in the crystal. Similar behaviour was found in other Li aluminosilicates [39].

Inspection of Fig. 1 further shows that a peak asymmetry, expected for the glass due to the correlated motion in a disordered system, is also found for the crystal. The deviation from standard SLR behaviour [16] is also reflected by a subquadratic frequency dependence of T_1^{-1} found on the low-T flank of the peak for both modifications [38]. Thus, in this regard the apparently ordered ion conductor shows nearly the same 'anomalies' as the disordered one.

Besides the main peak at about 820 K, in Fig. 1 a second, broad maximum can be seen for the crystalline sample around roughly 100 K. This can be attributed to the short-range hopping of the Li ions between the pair sites mentioned above. Fig. 2 shows the corresponding data obtained by β-NMR on ^{8}Li at 3 MHz [17] covering the temperature range from about 500 K down to 10 K. Whereas in the case of polycrystalline $LiAlSi_2O_6$ transients $P(t)$ of the ^{8}Li polarization could be fitted by a single exponential, in the glass

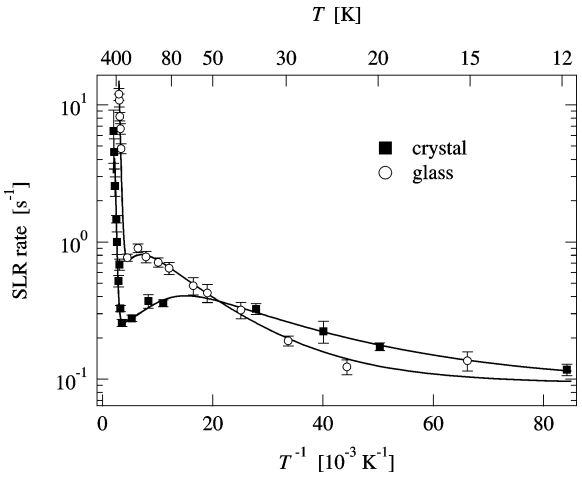

Fig. 2: Temperature dependence of the spin-lattice relaxation rate of ^{8}Li in glassy (○) and polycrystalline (■) $LiAlSi_2O_6$ (β-spodumene) at a magnetic field corresponding to $\omega_L/2\pi$ = 3 MHz [17]. The lines are drawn to guide the eye.

$P(t)$ followed the $\sqrt{t}$ behaviour expected for the highly diluted probe nuclei due to inhomogeneous polarization averaging [40]. The resulting values of the inhomogeneous relaxation rate T_{1inh}^{-1} are displayed in Fig. 2. For temperatures above 200 K the low-temperature flank of the long-range diffusion induced peak is visible again. The maximum of the relaxation rate due to the localized jumps in crystalline $LiAlSi_2O_6$ occurs at about 70 K. For the glassy material this maximum appears only as a slight shoulder.

Using the temperature of the SLR rate maximum of ^{7}Li together with that of ^{8}Li (Figs. 1 and 2) one can estimate the activation energy or the jumps between the pair sites in the crystalline material to be roughly 50 meV. This result is also consistent with ^{7}Li-T_1 data obtained at different frequencies [26].

In summary, glassy and crystalline spodumene provides a playground for the study of the influence of disorder on ion transport properties by complementary NMR techniques. Long-range and local motion showed up both in the crystal and in the glass. The local hopping in the glass could only be detected with the help of β-NMR.

4.2 Line Narrowing: Nanocrystalline Li_2O:Al_2O_3 Composites

Nanocrystalline oxides with particle sizes in the nm range are characterized by a heterogeneous structure consisting of nanosized crystalline grains with random crystallographic orientations and a high volume fraction of interfacial regions [41,42]. In single-phase nanocrystalline materials the charge carriers near or in the interfacial regions often show markedly increased diffusivity [43,44]. In two-phase nanocrystalline composites, such as Li_2O:X_2O_3 (X = B, Al), the effect of increased Li diffusivity may be additionally enhanced, which can be studied by ^{7}Li lineshape NMR spectroscopy [45,46].

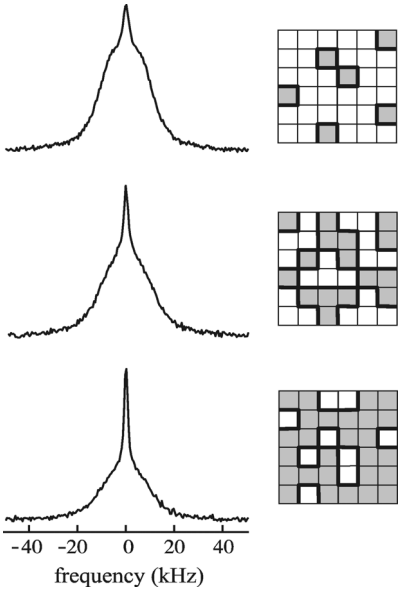

Fig. 3: ^{7}Li NMR spectra ($\omega_L/2\pi$ = 58.3 MHz) of nanocrystalline (1-x)Li_2O:xAl_2O_3 recorded at T = 433 K. The Li content is x = 0.2, 0.5, and 0.8, respectively (from top to bottom). Spectra are scaled to the same height. See text for further explanation.

The Li_2O:Al_2O_3 composites were prepared by high-energy ball milling of the coarse grained, i.e. microcrystalline, source materials [46]. According to x-ray diffraction line broadening the average particle diameter was about 25 nm for Li_2O and Al_2O_3.

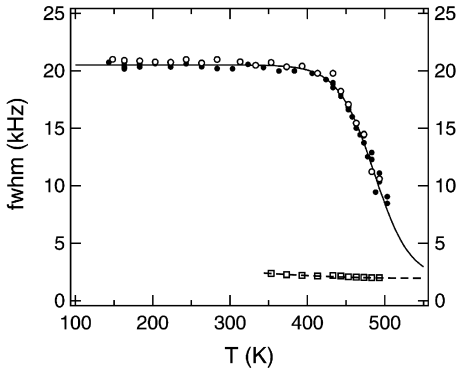

Fig. 4: NMR linewidths of the two signal contributions to the overall ^{7}Li NMR resonance of nanocrystalline (1-x)Li_2O:xAl_2O_3 with x = 0.5 in comparison with the linewidth of the corresponding microcrystalline composite, recorded at $\omega_L/2\pi$ = 58.3 MHz (after [46]). FWHM: full width at half maximum. (○,□) nanocrystalline, (●) microcrystalline. Lines are guides to the eye.

^{7}Li NMR measurements on the composite system (1-x)Li_2O:xAl_2O_3 were carried out at 58.3 MHz. In Li_2O with its antifluorite crystal structure, Li ions occupy empty tetrahedral sites formed by oxygen anions. The absence of any satellite peaks in ^{7}Li (I = 3/2) spectra of Li_2O single crystals and coarse grained samples indicate a nearly perfect tetrahedral symmetry. The following results will focus on the central transition. NMR spectra of composites Li_2O:Al_2O_3 with different Li contents x are shown in Fig. 3 at a temperature T = 433 K. All of them are composed of two contributions [46] with the same resonance frequency. The broad Gaussian shaped NMR line represents slow Li ions, whereas the motionally narrowed Lorentzian shaped contribution represents a sub-ensemble of Li ions being highly mobile at this temperature. In the NMR spectra of the corresponding microcrystalline composites as well as of pure microcrystalline Li_2O the narrow contribution is absent. These NMR spectra show a motional narrowing of the central transition identical to those of the broad contribution to the NMR line of the nano-composites. This is displayed in Fig. 4. Thus, it is concluded that the area fraction A_f of the narrow NMR line represents a subset of fast Li ions with enhanced diffusivity located in or near the interfacial regions. Furthermore, as A_f of the narrow NMR line increases with insulator content x (cf. Fig. 5), fast Li ions obviously reside in the interfacial regions between Li_2O and Al_2O_3 particles. In Fig. 3 the Li spectra have been compared with schemes of composites with different insulator contents, where the interfacial regions between unlike particles are represented by bold lines. Grey squares indicate insulator and white squares Li_2O particles. With increasing x the volume fraction of bold lines relative to the Li_2O content, and thus the fraction of mobile ions, increases with insulator content. In other words, the homo-interfaces between adjacent Li_2O particles are continuously replaced by hetero-interfaces between neighbouring Li_2O and Al_2O_3 particles being faster diffusion pathways for the Li ions. Remarkably, impedance spectroscopy measurements [47] show a maximum in dc conductivity at compositions with $x \approx 0.5$. This can be ascribed to the formation of highly diffusive percolation pathways by the hetero-interfaces at intermediate insulator contents (cf. Fig. 3). It should be noted that the two methods probe diffusion on different length scales, see Table 1.

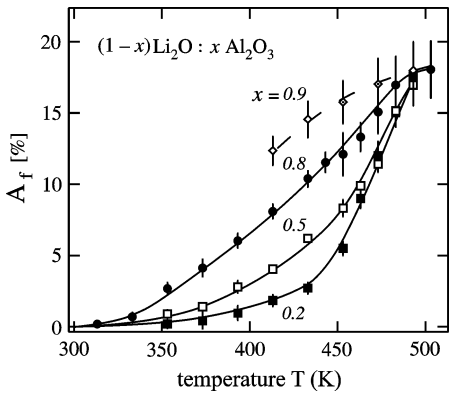

Fig. 5: Area fraction A_f of the narrow ^{7}Li NMR component (cf. Fig. 3) for different composites as a function of temperature. At high temperatures a saturation value of about 18% is reached.

As can be seen in Fig. 4, motional narrowing of the broad NMR component starts, i.e. averaging of local magnetic fields sets in, at about 450 K whereas narrowing of the contribution from the ions in the interfacial regions is already completed at this temperature (extreme motional narrowing). At 433 K the broad component shows still its rigid-lattice linewidth, indicating that the jump rates of Li ions in the grains are smaller than about 10^3 s^{-1}, while the ions in the interfacial regions are faster.

In Fig. 5 the area fraction of the narrow NMR line is plotted as a function of temperature for composites with different insulator contents. A_f and thus the number fraction of mobile ions increases continuously with increasing temperature and Al_2O_3 content x. At high temperatures A_f has attained about 18%, which appears to be a saturation value. This value reflects the mass fraction of the interfacial regions. It agrees with the value of about 15% which can be estimated assuming a thickness of 1 nm for the interfacial regions [41].

In summary, studying the heterogeneous Li diffusion in nanocrystalline materials is possible via NMR lineshape measurements. Due to their different transverse relaxation times and thus, because of different linewidths at a given temperature, the Li diffusion of the two different Li species can be studied separately [45,46].

4.3 Spin-Alignment Echo NMR: Extremely Slow Li Diffusion in $LiTiS_2$

Extremely slow Li jumps in the rigid-lattice range can be studied by recording spin-alignment echo amplitudes as a function of mixing time t_m. For example, in fully Li intercalated trigonal TiS_2 (space group $P\bar{3}m1$), extremely slow Li motions in the van der Waals gap between the TiS_2 layers can be detected in this way. At, e.g., 190 K the jump rate is about 3 s^{-1}.

In Fig. 6 the room-temperature spin-alignment echo amplitude $S_2(t_p,t_m,t = t_p)$ of $Li_{1.0}TiS_2$, taken at $t = t_p = 15$ μs, is shown in a semi-logarithmic plot as a function of mixing time varied over six decades. Between 293 K and 213 K the echo decay of $S_2(t_p, t_m)$ clearly proceeds in two steps. A sum of a stretched and a mono-exponential function for the first and the second step, respectively, is used to parameterize the S_2-curve shown in Fig. 6:

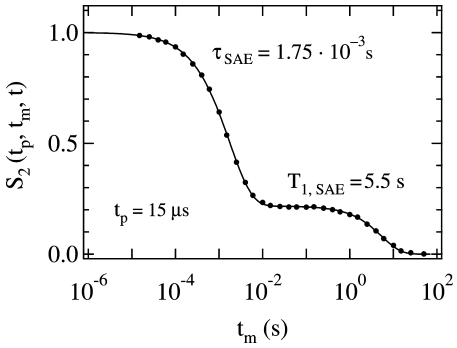

Fig. 6: SAE amplitude $S_2(t_p, t_m, t = t_p)$ of $Li_{1.0}TiS_2$ vs mixing time t_m. T = 293 K (after [25], t_p = 15 µs.) Data were recorded at a radio frequency of 155 MHz. The solid line corresponds to a fit according to Eq. (23).

$$S_2(t_m) = (1 - S_\infty) \exp\left(-\left(\frac{t_m}{\tau_{SAE}} \right)^{\beta} \right) + S_\infty \exp\left(-\frac{t_m}{T_{1,SAE}} \right) \quad . \tag{23}$$

The first step leads to a finite plateau value S_∞ at intermediate mixing times and is directly due to slow ionic jumps between inequivalent sites in the van der Waals gap, i.e. most likely between octahedral ($e^2 q^{oct} Q/h$ = 30 kHz) and tetrahedral sites ($q^{tetr} \neq q^{oct}$ [48]). Between 293 K and 200 K, the stretching exponent β varies from about 0.7 to 0.85 and the plateau value S_∞ turned out to be 0.22(1) at, e.g., t_p = 15 µs [25]. In general the plateau value S_∞ ($t_p \rightarrow \infty$) is related to the inverse number of inequivalent sites visited by the jumping ion. The relatively large value of S_∞ obtained here already at small evolution times indicates that only a small number of inequivalent sites is involved. Regarding the simple crystal structure of $Li_{1.0}TiS_2$, the most favorable diffusion pathway from octahedral to octahedral site entails the intermediate occupation of a tetrahedral site. Quite recently, this diffusion pathway was predicted by quantum chemical calculations [49] for Li migration in $TiSe_2$ which has the same crystal structure as TiS_2. The second step reflects the S_2-decay simply induced by spin-lattice relaxation.

Decay rates τ_{SAE}^{-1} obtained at 78 and 32 MHz as a function of inverse temperature $1/T$ are shown in Fig. 7. They exhibit an Arrhenius behaviour with an activation energy of 0.26(1) eV for the aforementioned hopping process. τ_{SAE} is, as expected for a motional correlation time, frequency independent. For comparison spin-lattice relaxation rates T_1^{-1} and spin-spin relaxation rates T_2^{-1} measured at 78 MHz are also displayed. Within the rigid lattice regime (140 K – 300 K) two sections can be differentiated. From 185 K to 300 K, the two time constants τ_{SAE} and $T_{1,SAE}$ can be well separated, because longitudinal relaxation proceeds on a much slower time scale than the spin-alignment decay. At lower temperatures, however, the temperature dependence of the decay rates follows that of T_1.

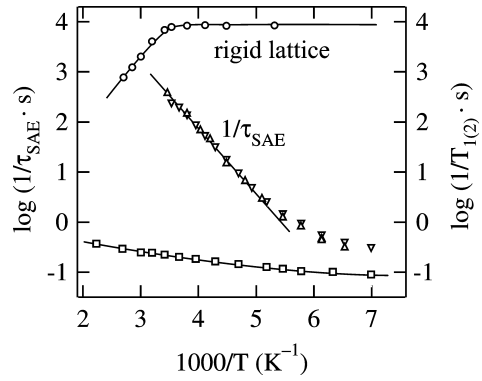

Fig. 7: Spin-alignment decay rates τ_{SAE}^{-1} vs reciprocal temperature obtained for two different radio frequencies (△) 32 MHz and (▽) 78 MHz. For comparison T_2^{-1} spin-spin (○) and T_1^{-1} spin-lattice relaxation rates (□) are shown, too.

Contrary to the spin-alignment data, the T_1^{-1} as well as T_2^{-1} relaxation rate data below 280 K do not reflect any diffusive ionic motion. Longitudinal relaxation is sensitive to hopping motions with jump rates of the order of the Larmor frequency, i.e. on the nanosecond time-scale. The T_1^{-1} data between 140 K and 300 K represent the so-called 'non-diffusive' background on which the diffusion induced $T_1^{-1}(1/T)$ peak is superimposed at higher temperatures [50]. We mention that in the case of $Li_{0.7}TiS_2$ the high-temperature flank of the T_1^{-1} peak shows the characteristic logarithmic frequency dependence [51] as a result of diffusion being confined to two dimensions, namely between the TiS_2 layers.

In summary, spin-alignment echo NMR spectroscopy has been used to detect extremely slow ionic motions in $LiTiS_2$, which are not accessible by conventional lineshape or spin-spin relaxation measurements. This method thus complements the dynamic range 10^{-1} … 10^9 s^{-1} covered by the microscopic NMR methods.

4.4 SFG and PFG NMR: Self-Diffusion in Solid Lithium

As a simple test case for the application of both SFG and PFG NMR on an identical solid sample, after upgrading a standard solid state NMR spectrometer to a low-cost combined SFG and PFG NMR spectrometer, we have measured the tracer diffusion coefficient of ^7Li in solid lithium (bcc structure) [52]. Starting near the melting point (454 K), the tracer diffusion coefficient was measured down to a temperature as low as possible. With SFG NMR the measurement of tracer diffusion coefficients has been possible in the range from 445 K down to 320 K. With PFG NMR the temperature range from 445 K down to 334 K was covered. In Fig. 8 the D^T data from SFG and PFG NMR are plotted versus reciprocal temperature. The values obtained by the two methods show good overall agreement. Deviations exist only in the low-temperature range. This can be due to the fact that for PFG NMR small differences in the shape of the two gradient pulses or insufficient mechanical decoupling may occur [52]. Disregarding the PFG NMR data points at temperatures below 365 K, for both methods the temperature dependence can be described by an Arrhenius relation (Eq. (4)) with an activation energy of 0.57 eV and $D_0^T = 2.3 \cdot 10^{-5}$ m^2/s. For temperatures below 334 K no PFG NMR measurements are possible because T_2 becomes too small.

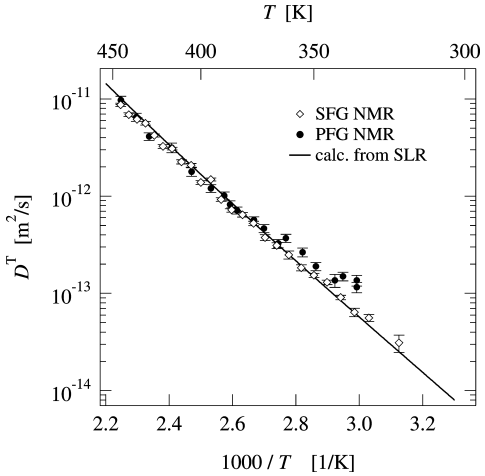

Fig. 8: Tracer diffusion coefficients of ^{7}Li in solid lithium versus inverse temperature measured by SFG and PFG NMR. The tracer diffusion coefficients determined from ^{8}Li spin-lattice relaxation (SLR) [53] were calculated under the assumption of a monovacancy-divacancy mechanism resulting in a weak upward curvature at high temperatures.

Comparison of our data with tracer diffusion data from the literature [54-56] shows good agreement. In particular, our SFG NMR data confirm small deviations from Arrhenius behaviour, i.e. a slightly increased slope at high temperatures [55]. This might hint at a change of the predominant diffusion mechanism [57]. A point of interest is whether these deviations exist for diffusion coefficients of uncorrelated diffusion D^{uc} as well. The ratio of the tracer diffusion coefficient D^T and D^{uc} is the correlation factor f (cf Eq. (7)). In the case of self-diffusion, which we are concerned with here, f is a constant depending on the crystal structure and the diffusion mechanism.

The coefficient of uncorrelated diffusion can be calculated with Eq. (6) from the jump rate τ^{-1} obtained by spin-lattice relaxation (SLR) measurements. These were done for solid lithium by ^{7}Li-NMR ([58] and references therein) and β-NMR on ^{8}Li [53,59]. Assuming a definite diffusion mechanism and adopting its characteristic correlation factor, a calculation of D^T from D^{uc} is possible. In case of Li self-diffusion in solid lithium a combined process of monovacancy and divacancy diffusion has been assumed [53,57-59]. Monovacancy (1V) diffusion in a bcc lattice has a correlation factor of f_{1V} = 0.727 and divacany (2V) diffusion has a correlation factor of, e.g., f_{2V} = 0.347 (2N-4N-2N configuration, i.e. hopping of the two vacancies via second nearest neighbour and fourth nearest neighbour sites) [60]. The tracer diffusion coefficient may then be expressed by

$$D^T = f_{1V} \cdot D_{1V}^{uc} + f_{2V} \cdot D_{2V}^{uc} \quad . \tag{24}$$

In Fig. 8 calculated tracer diffusion coefficients resulting from our earlier ^{8}Li T_1 data [53] are shown together with our measured tracer diffusion coefficients. Isotope effects of ^{7}Li/^{8}Li diffusion are not relevant as shown in [54]. It is concluded that the assumed monovacancy-divacancy diffusion mechanism is consistent with our field gradient NMR results.

From the methodical point of view, both methods, SFG and PFG NMR, have their own specific area of application [52]. PFG NMR is favourable for small magnetogyric ratios γ and long relaxation times T_2 which is valid for many solids above room

temperature. SFG NMR is preferred for large γ and short relaxation times T_2, hence for solids around and below room temperature. Therefore, SFG and PFG NMR are to be regarded as complementary methods. For both methods holds that the smaller the diffusion coefficients the larger the necessary gradients are.

5. Conclusion

In this review we have demonstrated that for the investigation of diffusion in solids nuclear magnetic resonance provides an arsenal of various techniques. On the one hand atomic jump rates have been studied over ten decades from 10^9 s^{-1} down to 10^{-1} s^{-1} by microscopic NMR methods. On the other hand macroscopic tracer diffusion coefficients in solids have been accessible down to about 10^{-14} m^2s^{-1} by field gradient NMR techniques, which traditionally are applied to liquids. Both has been exemplified by studies from our laboratory. These include comparative measurements on glassy and crystalline $LiAlSi_2O_6$ by NMR as well as β-NMR spin-lattice relaxation, a study of heterogeneous spin-spin relaxation (or linewidths) in the nanocrystalline ionic conductor/insulator composite Li_2O:Al_2O_3, spin alignment decay measurements of ultraslow motion in the layered compound $LiTiS_2$, and finally a comparative study by static and pulsed field gradient NMR on solid lithium as a simple model system. In the latter case, the temperature dependence of the obtained tracer diffusion coefficients has also been used for a comparison with that of the uncorrelated diffusion coefficient derived from β-NMR spin-lattice relaxation measurements in order to get information on the underlying diffusion mechanism.

References

[1] W. Jost, Diffusion in Solids, Liquids, Gases, Academic Press, New York, 1960.
[2] J. Philibert, Atom Movements – Diffusion and Mass Transport in Solids, Les Editions de Physique, Les Ulis, 1991.
[3] P. Heitjans, J. Kärger (Eds.), Diffusion in Condensed Matter – Methods, Materials, Models, Springer, Berlin, 2005.
[4] P. Heitjans, Solid State Ionics 18/19 (1986) 50.
[5] P. Heitjans, S. Indris, J. Phys.: Condens. Matter 15 (2003) R1257.
[6] H. Mehrer, Chap. 1 in [3].
[7] J. Crank, The Mathematics of Diffusion, Clarendon Press, Oxford, 1975.
[8] A. Einstein, Ann. Phys., Lpz. 17 (1905) 549.
[9] M. von Smoluchowski, Ann. Phys., Lpz. 21 (1906) 756.
[10] A. Bunde, W. Dieterich, P. Maass, M. Meier, Chap. 20 in [3].
[11] K. Funke, C. Cramer, D. Wilmer, Chap. 21 in [3].
[12] H. Schmalzried, Chemical Kinetics of Solids, VCH, Weinheim, 1995.
[13] A. Abragam, The Principles of Nuclear Magnetism, Clarendon Press, Oxford, 1961.
[14] C.P. Slichter, Principles of Magnetic Resonance, Springer, Berlin, 1989.
[15] A.R. Allnatt, A.B. Lidiard, Atomic Transport in Solids, Cambridge Univ. Press, Cambridge, 1993.
[16] N. Bloembergen, E.M. Purcell, R.V. Pound, Phys. Rev. 73 (1948) 679.
[17] P. Heitjans, A. Schirmer, S. Indris, Chap. 9 in [3].

[18] H. Ackermann, P. Heitjans, H.-J. Stöckmann, in: J. Christiansen (Ed.), Hyperfine Interactions of Radioactive Nuclei, Topics in Current Physics, vol 31, Springer, Berlin, 1983, pp. 291-361.
[19] P. Heitjans, W. Faber, A. Schirmer, J. Non-Cryst. Solids 131-133 (1991) 1053.
[20] M. Vogel, C. Brinkmann, H. Eckert, A. Heuer, Phys. Chem. Chem. Phys. 4 (1995) 3237; M. Vogel, Phys. Rev. B 68, (2003) 184301; M. Vogel, C. Brinkmann, H. Eckert, A. Heuer, Rev. B 69 (2004) 094302.
[21] H.W. Spiess, J. Chem. Phys. 72 (1980) 6755 .
[22] X.-P. Tang, R. Busch, W.L. Johnson, Y. Wu, Phys. Rev. Lett. 81 (1998) 5358; X.-P. Tang, U. Geyer, R. Busch, W.L. Johnson, Y. Wu, Nature 402 (1999) 160. X.-P. Tang, Y. Wu, J. Magn. Res. 133 (1998) 155.
[23] F. Qi, T. Jörg, R. Böhmer, Solid State Nucl. Magn. Reson. 22 (2002) 484.
[24] F. Qi, G. Diezemann, H. Böhm, J. Lambert, R. Böhmer, J. Magn. Reson. 169 (2004) 225.
[25] M. Wilkening, P. Heitjans, Defect Diffus. Forum 237-240 (2005) 1182.
[26] F. Qi, C. Rier, R. Böhmer, W. Franke, P. Heitjans, Phys. Rev. B, accepted
[27] J. Jeener, P. Broekaert, Phys. Rev. 157 (1967) 232.
[28] R. Böhmer, J. Magn. Res. 147 (2000) 78.
[29] R. Kimmich, W. Unrath, G. Schnur, E. Rommel, J. Magn. Reson. 91 (1991) 136.
[30] H.Y. Carr, E.M. Purcell, Phys. Rev. 94 (1954) 630.
[31] C.P. Slichter, Principles of Magnetic Resonance, Springer Verlag, Berlin, 1996.
[32] B. Geil, Concepts Magn. Reson. 10 (1998) 299.
[33] J.E. Tanner, J. Chem. Phys. 52 (1970) 2523.
[34] J. Kärger, H. Pfeifer, W. Heink, in: J.S. Waugh (Ed.), Advances in Magnetic Resonance vol. 12, Academic Press, New York, 1988, pp.1-89.
[35] R. Kimmich, NMR – Tomography, Diffusometry, Relaxometry, Springer, Berlin, 1997.
[36] J. Kärger, F. Stallmach, Chap. 10 in [3].
[37] W.S. Price, Concepts Magn. Reson. 9 (1997) 299.
[38] W. Franke, P. Heitjans, Ber. Bunsenges. Phys. Chem. 96 (1992) 1674.
[39] R. Winter, K. Siegmund, P. Heitjans, J. Non-Cryst. Solids 212 (1997) 215.
[40] H.-J. Stöckmann, P. Heitjans, J. Non-Cyst. Solids 66 (1984) 501.
[41] R.W. Siegel, in G.L. Trigg (Ed.), Encyclopedia of Applied Physics, VCH, Berlin, 1994.
[42] H. Gleiter, Prog. Mater. Sci. 33 (1989) 223.
[43] M. Wilkening, D. Bork, S. Indris, P. Heitjans, Phys. Chem. Chem. Phys. 4 (2002) 3246.
[44] M. Masoud, P. Heitjans, Defect Diffus. Forum 237-240 (2005) 1016.
[45] S. Indris, P. Heitjans, J. Non-Cryst. Solids 307-310 (2002) 555.
[46] M. Wilkening, S. Indris, P. Heitjans, Phys. Chem. Chem. Phys. 5 (2003) 2225.
[47] S. Indris, P. Heitjans, H.E. Roman, A. Bunde, Phys. Rev. Lett. 84 (2000) 2889; S. Indris, P. Heitjans, M. Ulrich, A. Bunde, Z. Phys. Chem. 219 (2005) 89.
[48] T. Bredow, P. Heitjans, M. Wilkening, Phys. Rev. B 70 (2004) 115111.
[49] C. Ramírez, R. Adelung, R. Kunz, L. Kipp, W. Schattke, Phys. Rev. B 71 (2005) 035426.

[50] W. Küchler, Dissertation, Universität Hannover, 1993.
[51] W. Küchler, P. Heitjans, A. Payer, R. Schöllhorn, Solid State Ionics 70/71 (1994) 434.
[52] D.M. Fischer, P. Duwe, S. Indris, P. Heitjans, Solid State Nucl. Magn. Reson. 26 (2004) 74.
[53] P. Heitjans, A. Körblein, H. Ackermann, D. Dubbers, F. Fujara, H.-J. Stöckmann, J. Phys. F: Met. Phys. 15 (1985) 41.
[54] M. Mali, J. Roos, M. Sonderegger, D. Brinkmann, P. Heitjans, J. Phys. F: Met. Phys. 18 (1988) 403.
[55] R. Messer, A. Seeger, K. Zick, Z. Metallkd. 80 (1989) 299.
[56] A. Lodding, J.N. Mundy, A. Ott, Phys. Status Solidi 38 (1970) 559.
[57] A. Seeger, Defect Diffus. Forum 143-147 (1997) 21.
[58] R. Messer, F. Noack, Appl. Phys. 6 (1975) 79.
[59] A. Körblein, P. Heitjans, H.-J. Stöckmann, F. Fujara, H. Ackermann, W. Buttler, K. Dörr, H. Grupp, J. Phys. F: Met. Phys. 15 (1985) 561.
[60] H. Mehrer, J. Phys. F: Metal Phys. 3 (1973) 543.